Journal of Materials Chemistry A

Creating compressive stress at the NiOOH/NiO interface for water oxidation

Journal:	*Journal of Materials Chemistry A*
Manuscript ID	TA-COM-04-2020-004244.R1
Article Type:	Communication
Date Submitted by the Author:	07-May-2020
Complete List of Authors:	Kuai, Chunguang; Virginia Polytechnic Institute and State University, Chemistry; Tianjin University, Institute of New-Energy Materials, School of Materials Science and Engineering Zhang, Yan; Tianjin University, Institute of New-Energy Materials, School of Materials Science and Engineering; SLAC National Accelerator Laboratory Han, Li-Li; University of California Irvine, Department of Physics and Astronomy Xin, Huolin; University of California Irvine, Department of Physics and Astronomy Sun, Chengjun; Argonne National Laboratory Advanced Photon Source Nordlund, Dennis; Stanford Synchrotron Radiation Lightsource Qiao, Shizhang; The University of Adelaide, School of Chemical Engineering Du, Xiwen; Tianjin University, Institute of New-Energy Materials, School of Materials Science and Engineering Lin, Feng; Virginia Polytechnic Institute and State University, Chemistry

COMMUNICATION

Creating compressive stress at the NiOOH/NiO interface for water oxidation

Received 00th January 20xx,
Accepted 00th January 20xx

DOI: 10.1039/x0xx00000x

Chunguang Kuai, [a, b] Yan Zhang, [b, c] Lili Han, [d] Huolin L. Xin, [d] Cheng-Jun Sun, [e] Dennis Nordlund, [c] Shizhang Qiao, [f] Xi-Wen Du, *[b] Feng Lin *[a]

AbstractEnhancing the oxygen evolution reaction (OER) performance of NiO materials will greatly expand their applications as low-cost, bifunctional electrocatalysts for water splitting reactions. Introducing stress into the surface layer of catalysts represents an effective method to enhance their catalytic reactivity. Herein, we create compressive stress at the NiOOH/NiO interface using the battery conversion chemistry and *in situ* Ni to NiOOH transformation. As a result, the OER performance is enhanced by 20 folds compared with that of the pure NiO. However, due to the corrosive environment that the electrocatalyst experience under OER conditions, the stress is released after several CV cycles. The present study demonstrates the importance of interfacial stress that can be produced from the *in situ* surface phase transformation of the electrocatalyst, as well as highlights the challenge of maintaining the mechanical stress under OER conditions during long-term applications.

The main text of the article should appear here. Headings and subheadings are not permitted in articles submitted to *Chemical Communications* although they are permitted in communications submitted to other journals.

Nickel oxide based materials are promising multifunctional electrocatalysts for rechargeable batteries and hydrogen electrolyzers[1-10], especially for water oxidation that is usually the rate-limiting reaction for energy storage and conversion[11-13]. In principle, an optimal electrocatalyst should adsorb intermediates neither too strong nor too weak[14, 15], however, Ni based oxides catalysts possess excessively high adsorption capabilities for OER intermediates, which extensively limits their catalytic performance[16, 17].

Lattice strain is an effective strategy for improving the adsorption energy and catalytic performance[18-21]. For transition metal oxides, lattice strain can modify the metal-oxygen coordination, then electron filling in e_g orbitals, and eventually adsorption energy[22, 23]. A common methodology for creating lattice strain is to construct interface between two phases with different lattice parameters[21, 24, 25]. During OER process, an oxyhydroxide layer usually forms on the surface of transition metal oxide and serves as the active phase[26-31]. The lattice mismatch between oxide and oxyhydroxide causes distortion and strain in both sides, which can modulate the OER performance. However, a fierce surface reconstruction may occur during the surface phase transformation of metal oxide, including metal-oxygen bond breaking, crystal symmetry breakdown, and lattice oxygen loss[27, 29, 32], leading to an amorphous surface layer and the release of mechanical stress. Thus, it is of importance to grow well crystallized oxyhydroxide on the oxide catalyst so as to create lattice strain for boosting OER performance.

In this work, we electrochemically reduce NiO nanosheets partially to produce Ni nanoparticles on the pristine NiO substrate. Subsequently, the Ni nanoparticles are transformed into highly crystalline $Ni(OH)_2$ nanoparticles at elevated overpotentials, and further into NiOOH through a deprotonation process at the OER relevant potential. The strong interaction between the crystalline NiOOH and NiO builds up interfacial stress. As a result, the current density at 1.63V vs RHE shows about a 20-fold enhancement compared to that of the NiO/NiOOH counterpart without stress during the inaugural cycles. Our work provides a new method for enhancing the OER activity through interfacial strain. We also note the challenge of maintaining the mechanical stress for long-term durability.

Experimental

[a] *Department of Chemistry, Virginia Tech, Blacksburg, VA 24061, USA. Email: fenglin@vt.edu*
[b] *Institute of New-Energy Materials, School of Materials Science and Engineering, Tianjin University, Tianjin, 300072, China. Email: xwdu@tju.edu.cn*
[c] *Stanford Synchrotron Radiation Lightsource, SLAC National Accelerator Laboratory, Menlo Park, California 94025 , USA*
[d] *Department of Physics and Astronomy, University of California, Irvine, CA 92697, USA*
[e] *Advanced Photon Source, Argonne National Laboratory, Argonne, Illinois 60439, USA*
[f] *School of Chemical Engineering, The University of Adelaide, Adelaide, SA 5005, Australia*

Electronic Supplementary Information (ESI) available: [details of any supplementary information available should be included here]. See DOI: 10.1039/x0xx00000x

The rocksalt NiO nanosheets were synthesized according to the method reported elsewhere[33, 34]. The details are as follows. $Ni(NO_3)_2$•6 H_2O, urea and benzyl alcohol were mixed with the weight ratio of 2:1:4 and then dissolved in 50mL methanol with vigorous stirring for 1 hour. The solution was then transferred to an autoclave. Before heating, the mixture was purged with Ar for 5 min. Ar was filled to a pressure of 9 bars. Then the mixture was heated to 265 ℃ and maintained for 1.5h. The vapor was then vented, and a green powder was collected. The powder was calcined at 500 ℃ for 6 h to yield NiO nanosheets.

The morphologies of the materials were investigated using a scanning electron microscope (SEM) (JEOL JSM-7000F). High-angle annular dark-field scanning transmission electron microscopy (HAADF-STEM) was acquired on S/TEMs operated at 200 and 300 keV. Transmission electron microscopy (TEM) was operated on a JEOL JEM 2100: Thermal emitter (LaB_6) scanning TEM.

The electrode was prepared through a dip casting method. First, 1 mg catalyst was dispersed in 0.5 ml water, and then mixed with 0.5 ml methanol and 20 **μ**l 5% Nafion solution. The mixtures were ultrasonically dispersed for about 3 hours to form a catalyst ink. 20 **μ**l of catalyst ink was carefully dropped onto a 0.5*0.4 cm^2 carbon paper electrode, with a mass loading of about 0.1 mg/cm^2. Then the catalyst-coated electrodes were dried at room temperature for about 1 h. The sample was first discharged in 1 M $LiPF_6$ electrolyte solution in 1:1 w/w ethylene carbonate/diethyl carbonate, with Na foil as the counter/reference electrode in a Ar-filled glovebox. The test was performed through a MACCOR model 4200M workstation. The discharge rate was set to 1C with a theoretical capacity of 718 mAh/g. After discharging, the sample was washed with de-ion water to remove the electrolyte and sodium oxide. The detailed procedure for cleaning the sample is as follows. We first immersed the sample in the DI water for about 12 hours to remove the water soluble salts and most of the organic electrolyte on the electrode, and then the possible liquid electrolyte residue is removed during the drying process of the electrode. After through cleaning of the electrode, both electrolyte and sodium oxide should be minimized to a very low content. The influence of these residues on the OER performance should be minimal.

We then conducted CV measurement using a Biologic SP150 electrochemistry workstation in O_2 saturated 1M KOH electrolyte. A graphite rod and a Ag/AgCl electrode are used as the counter and reference electrodes, respectively. The following equation is used to convert the applied potential between Ag/AgCl and reversible hydrogen electrode (RHE):

$$E(RHE) = E(Ag/AgCl) + 0.059pH + 0.197V$$

The scan rate for the CV test was set to be 5 mV s^{-1}.

All the soft XAS measurements were carried out at the Stanford Synchrotron Radiation Lightsource, SLAC National Accelerator Laboratory. Soft XAS for Ni L-edge and O K-edge was performed at Beam Line 10-1. Samples for ex-situ soft XAS were mounted on a ¾ inch Al stick at an angle of about 55° with respect to the incident beam. A 1,000 l mm^{-1} spherical grating monochromator with 20 μm entrance and exit slits were applied to provide ~10^{11} ph s^{-1} at 0.2 eV resolution in a 1 mm^2 beam spot.

All the hard XAS were measured at beamline 20-ID at the Advanced Photon Source, Argonne National Laboratory. For all ex-situ experiments, samples were prepared on carbon paper (Toray Carbon Paper 090, The Fuel Cell Store) in a manner similar to that for electrochemical tests, removing Nafion to prevent undesired interference. The Ni K-edge spectra were collected in the fluorescence mode with the samples aligned at an angle of ~45° with respect to the incident beam and the Lytle detector. To minimize the background from elastic and Compton scattering, *Z-1* filters (e.g. Co filter for Ni K-edge) with Soller slits were placed before the window of the detector. Pure metal foils were used to align E_0 to 8333eV for Ni. The energy resolution for the collected spectroscopy is around 0.1eV.

Synchrotron XRD measurements were carried out at beamline 11-3 at the Stanford Synchrotron Radiation Lightsource, SLAC National Accelerator Laboratory. LaB_6 was used as the standard material for calibration. The exposure time was set as 0.5s to avoid any saturation. The wavelength of the synchrotron X-ray is 0.9762 Å, with the Bragg equation: 2d sinθ = nλ, the collected pattern was converted to the Lab X-ray pattern using Cu Kα as X-ray source (wavelength = 1.5406 Å).

The operando UV-vis measurement was conducted through an Ocean optics miniature spectrometer. The samples were spray coated on an FTO glass, forming a gray layer on the glass. The CV scans were conducted by a Biologic SP150 potentiostat, with a Pt wire as the counter electrode and Ag/AgCl as the reference electrode. The potential range was set to be 0.1-0.6V vs. Ag/AgCl. The applied potential was converted to the reversible hydrogen electrode (RHE) potential with the following equation:

$$E(RHE) = E(Ag/AgCl) + 0.059pH + 0.197V$$

The UV-vis was measured in the absorbance mode. Spectra were collected at 500 nm.

Results and discussion

NiO is synthesized using a solvothermal method aided with a pseudo-supercritical drying technique[33]. The as-prepared material exhibits a nanosheet morphology with hexagonal holes (Fig. 1a,b). Synchrotron X-ray diffraction (XRD) and hard X-ray absorption spectroscopy (XAS) reveal that the material is strictly rocksalt-phase NiO with Ni cations in the +2 oxidation state (Fig. S1, 1f). High resolution HAADF-STEM imaging shows a hexagonal arrangement of nickel ion columns (Fig. 1c), indicating that the exposed surfaces are mainly NiO (111). The (111) surface exposure is also confirmed by comparing the fast Fourier transform (FFT) pattern of the high resolution HAADF-STEM image with the simulated electron diffraction pattern of rocksalt NiO along the [111] zone axis (Fig. S2). To *in situ* grow Ni nanoparticles on the NiO surface, we assemble a sodium ion battery with the NiO powder as the cathode and sodium foil as the anode[34-36]. The discharge capacity is around 280 mAh/g at 1C, far below the theoretical capacity (~718 mAh/g) (Fig. 1d). The capacity discrepancy is originated from the surface passivation during the electrochemical sodiation, inhibiting the

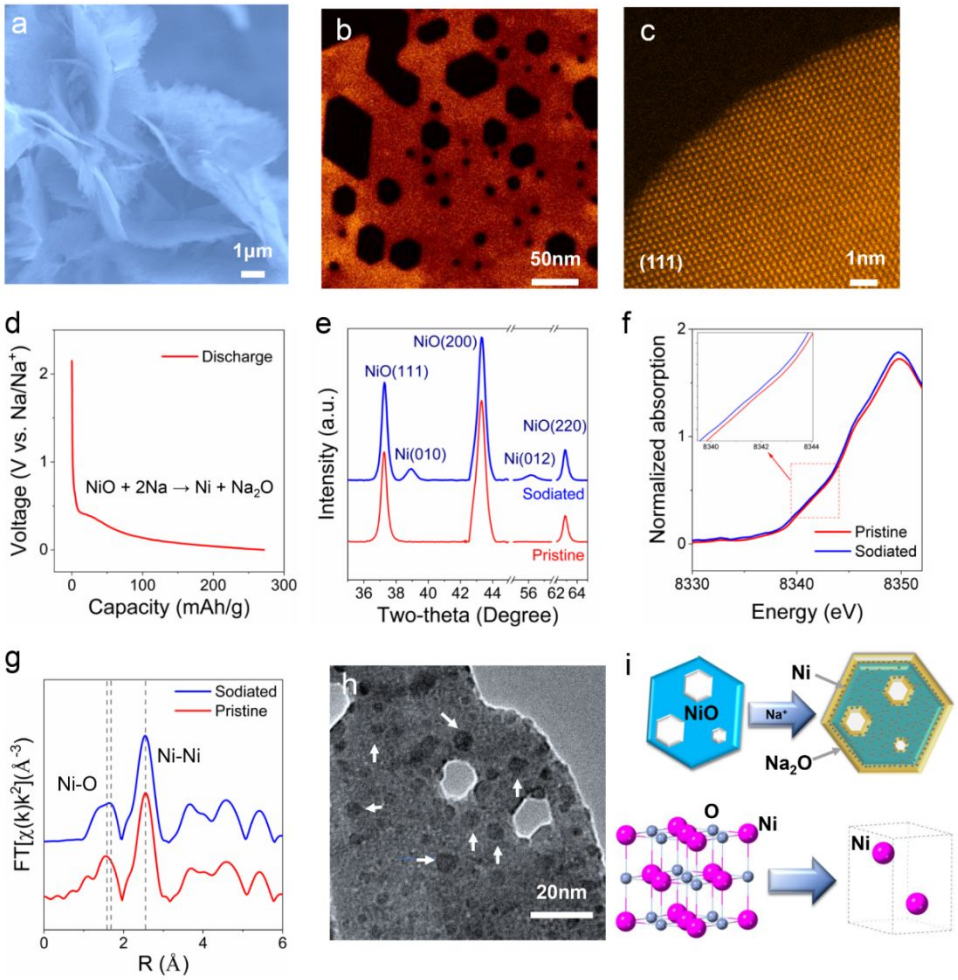

Figure 1 Characterization of the pristine and sodiated NiO nanosheet. a) SEM image of the pristine NiO. b) HAADF-STEM image of the pristine NiO. c) High resolution HAADF-STEM image of the pristine NiO. d) Discharge curve of the pristine NiO at 1C in a Na metal cell. e) Synchrotron XRD patterns for the pristine and sodiated NiO. The samples are loaded on the carbon paper. Peaks from the carbon paper are subtracted from the as-collected pattern. f) Hard XAS of the pristine and sodiated NiO. Insert is the enlargement of the K edge around the absorption value 0.5. g) The Fourier transformation of the extended X-ray absorption fine structure (EXAFS). h) BF-TEM image of the sodiated NiO, where the arrows point to Ni nanoparticles. i) Scheme for the formation of Ni nanoparticles on the surface of NiO nanosheet.

complete transformation of NiO to Ni[34]. In addition, we believe that part of the discharge capacity is attributed to the electrolyte decomposition and SEI formation[33, 34, 36]. Furthermore, to create electrodes for the OER catalysis, we use a low mass loading NiO electrode, thus the discharge capacity may have been overestimated. Nevertheless, we observe a sloping voltage profile that hits near 0 V vs Na/Na^+, demonstrating that the NiO surface is partially reduced. The high-resolution synchrotron XRD shows that the resulting Ni nanoparticles exhibit a hexagonal crystal structure (Fig. 1e). The XRD peaks around 39˚ and 58˚ can be assigned to the (010) and (012) planes of hexagonal nickel metal crystals (Fig. 1h)[37, 38], which is produced by a reductive transformation from the original NiO nanosheet. The Ni K-edge hard XAS shows a slight red shift after sodiation, indicating the partial reduction of the NiO nanosheet, further confirming the formation of the surface Ni nanoparticles (Fig. 1f). The Fourier transformation of the

extended X-ray absorption fine structure (EXAFS) reveals that after sodiation, the peak representing the Ni-O bond becomes wider, resulting from the crystal symmetry breakdown, loss of the lattice oxygen, and formation of Ni nanoparticles (Fig. 1g). The schematic representation for the nickel metal formation is illustrated in Fig. 1i. With our electrochemical method, the formed sodium oxide acts as a passivation layer preventing the complete NiO reduction, resulting in the formation of fine Ni nanoparticles at the surface of the NiO nanosheet[34]. The as-prepared Ni nanoparticles inherit the close-packed structure of the original NiO, with the Ni arrangement changing from ABCABC to ABAB. Therefore, our experimental results imply a highly coherent interface has formed between Ni and NiO phases (Fig. 1i). Subsequently, we collect the sodiated NiO electrode and remove Na_2O and electrolyte through extensive DI water rinsing.

To investigate the influence of the formed Ni/NiO interface on the OER performance, we perform cyclic voltammetry (CV) measurements on the pristine and sodiated NiO samples. The current of the sodiated sample is around 20 times higher than that of the pristine NiO sample at 1.63 V vs. RHE (Fig.2 a, b), indicating much higher OER performance for the sodiated sample. The Tafel slope for the sodiated sample is smaller than the pristine counterpart at different CV cycles (Fig. 2c), which indicates the higher kinetics for the OER of the sodiated sample. The OER current is relatively stable for the pristine NiO during 10 CV cycles, whereas clear differences are observed between different cycles for the sodiated sample (Fig. 2 a, b and d). The OER performance increases initially and reaches a peak in the 5th cycle, and then it gradually decreases during the subsequent cycles. The area of the $Ni^{2+}/Ni^{3+/4+}$redox peak (insets in Fig. 2 a, b) before the OER takeoff voltage (~1.6 V) shows a gradual increase with the increasing cycle number for both pristine and sodiated NiO samples, indicating a gradual oxidation of Ni cations. It has been reported that the oxidation of Ni^{2+} to Ni^{4+} is a perquisite for the initiation of OER[39-42]. Thus, the OER current should linearly corelated with the amount of Ni^{4+} if all of the Ni sites are OER reactive. However, in our case, the OER current for both pristine and sodiated samples does not increase with the intensification of the $Ni^{2+}/Ni^{3+/4+}$ oxidation peak (Fig. 2d). The possible reason is that not all of the Ni sites are responsible for OER and that only the Ni sites at the surface are responsible for the OER. These results imply that the performance enhancement in the first five cycles of the sodiated NiO does not directly originate from the increasing Ni redox charge.

To obtain an insight into the transformation of the catalysts, we conduct an *operando* UV-Vis measurement. We monitor the absorption change at 500 nm for both pristine and sodiated sample, since this peak can represent the transformation between Ni hydroxide and oxyhydroxide[40, 43]. The absorption increase at 500 nm can be assigned to the formation of the Ni oxyhydroxide phase in the positive scan. In the negative scan, the absorption gradually decreases, representing the reduction of the Ni oxyhydroxide (Fig. 3a). These results confirm the

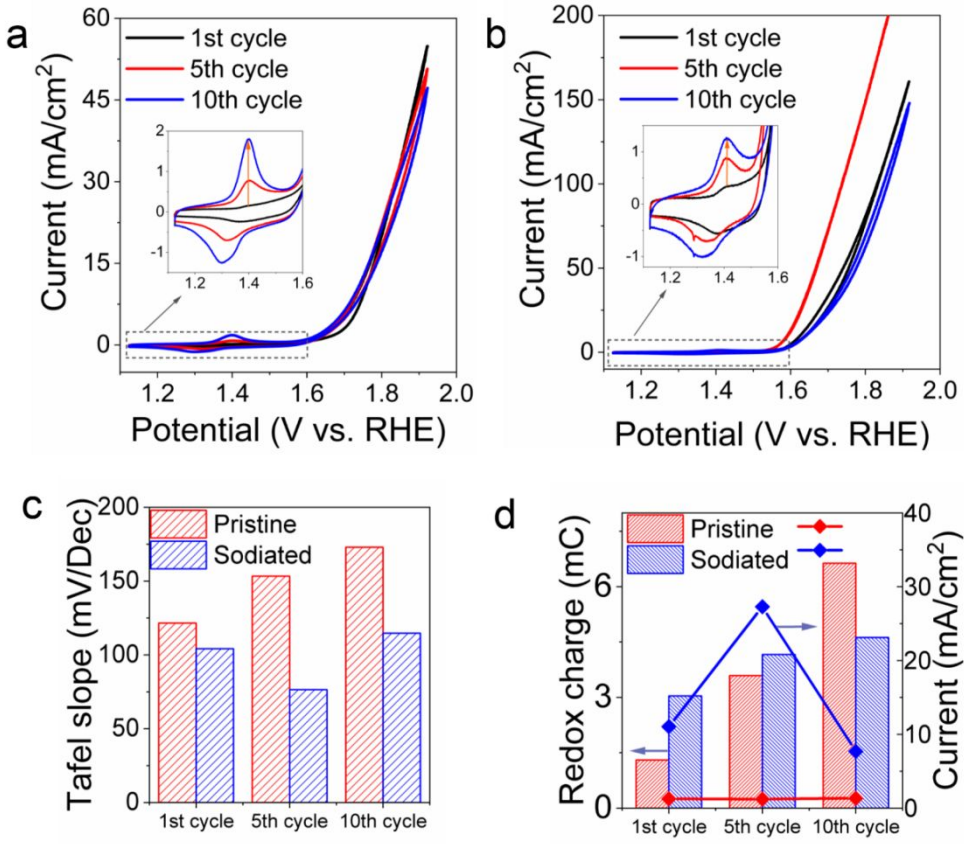

Figure 2 Electrochemical performance of the pristine and sodiated NiO. a, b) CV scan of the pristine and sodiated NiO, where the scan rate is 5mV/s. The Ni2+/Ni3+/4+ redox peaks are shown in the inserted figures. c) Tafel slope of the pristine and sodiated NiO at different CV cycles. d) The relationship between the Ni oxidation charge and the current density at 1.63V vs. RHE at different CV cycles. The redox charge is present as bar chart. The current is present as line chart. For both pristine and sodiated samples, the current density is not linearly related with the oxidation charge.

formation of Ni oxyhydroxide at the OER related potential. Furthermore, the absorption increases with the cycle number, which indicates the increased formation of Ni oxyhydroxide and is consistent with the redox charge calculation in Fig 2d.

redistribution of electrons (or holes) between Ni and O. We then use the change of the O K edge to detect the surface transformation of NiO during OER. The pre-edge peak of the O K-edge represents the Ni_{3d}-O_{2p} hybridization, which is related to

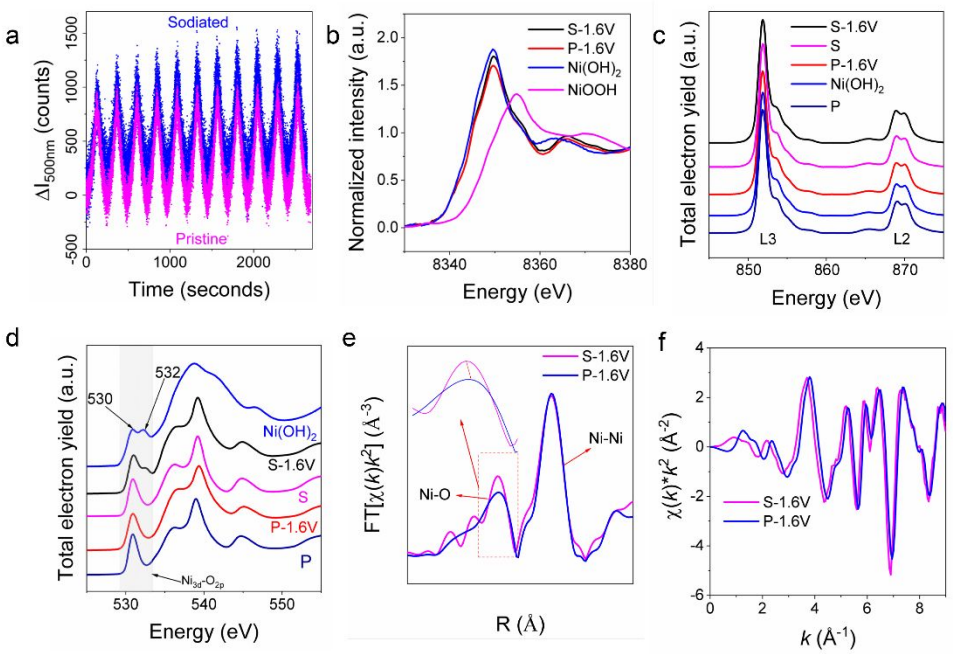

Figure 3 Structural changes of the NiO nanosheet after electrochemical test. a) Operando UV-vis test for the pristine and sodiated NiO during CV test for 10 cycles. The CV scan rate is 5mV/s. The absorption at 500 nm is collected during the CV scan. b) Ni K-edge for the pristine and sodiated sample before and after CA test. P and S represent pristine and sodiated, respectively. NiOOH and Ni(OH)2 are used as the standard materials for comparison. c and d) Soft XAS collected at a surface sensitive total electron yield (TEY) mode for the pristine and sodiated NiO before and after CA test at 1.6V vs. RHE. Ni(OH)2 is used as a standard material to investigate the surface structural change. e) EXAFS of the pristine and sodiated samples after the CA test in the R space. f) EXAFS of the pristine and sodiated samples after the CA test in the k space.

To get more insights into the performance enhancement and the distinct behaviors between different cycles of the sodiated sample, we further investigate the valence state change and phase transformation after the chronoamperometry (CA) measurement using hard XAS and soft XAS (Fig. 3b and 3c). The $Ni(OH)_2$ and NiOOH are used as references. The results show that the Ni K-edge positions show negligible differences compared with that of $Ni(OH)_2$ for both the pristine and sodiated samples after the CA measurement (Fig. 3b), which means that the valance states of Ni are 2+ after the release of the applied potential. As the water oxidation process takes place at the surface of the catalyst, we also investigate the surface transformation of the samples using soft XAS in the surface sensitive total electron yield (TEY) mode. The shapes and intensities of the Ni L_3 and L_2 peaks are similar for NiO and sodiation NiO either before or after the CA measurement (Fig.3c), which further confirms that the Ni valent state is Ni^{2+} at the surface. This result also suggests that the small fraction of Ni nanoparticles formed at the surface does not seem to impact the line shape of the Ni L-edge. During the CA test, the NiO at the surface can be oxidized to NiOOH. While after the test, the formed NiOOH could be easily reduced to $Ni(OH)_2$ through a protonation process in the electrolyte[44]. This will lead to the variation of the Ni coordination environment and thus the the Ni oxidation state and the Ni-O coordination environment. The pre-edge peaks for the pristine and sodiated samples are similar (Fig. 3d), indicating that the surface oxygen did not change too much during the sodiation process. After the CA test at 1.6 V vs. RHE, a new peak at ~532 eV appears for the sodiated sample. Meanwhile, the peak at ~530 eV for the pristine sample becomes wider (Fig. 3d). The peak deconvolution results show that there is indeed a peak formation at ~532 eV (Fig.S3). As the Ni oxidation state does not change, these pre-edge changes should be related to the Ni-O coordination environment change. After comparing with the pre-edge peak of a standard $Ni(OH)_2$, which show two well separated peaks at around 530 and 532eV (Fig. 3d), these pre-edge changes should be related to the formation of Ni-OH species at the surface. In summary, the surface for both pristine and sodiated samples will be oxidized to NiOOH upon oxidation and reduced to $Ni(OH)_2$ upon reduction, forming an interface between the $Ni(OH)_2$/NiOOH and NiO. The $Ni(OH)_2$/NiOOH formed at the surface of NiO can be either amorphous or crystalline. The crystalline transformation may introduce stress to the surface layer due to the lattice mismatch. High-resolution TEM shows that crystalline nanoparticles are formed after the CV test for the sodiated sample (Fig. S4), which may be formed through the direct transformation from Ni metal to NiOOH during OER. It is

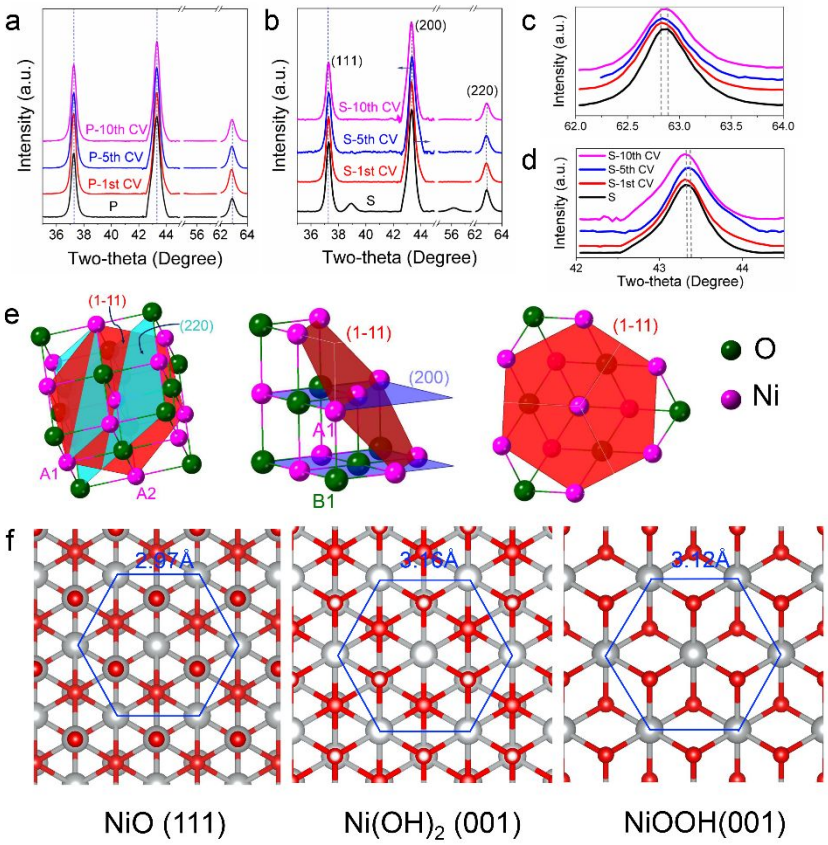

Figure 4 Stress analysis of the NiO nanosheet after electrochemical test. a) Synchrotron XRD for the pristine NiO after different CV cycles. b) Synchrotron XRD for the sodiated NiO after different CV cycles. c) (220) peak position shift for the sodiated sample at different CV cycles. d) (200) peak position shift for the sodiated sample at different CV cycles. e) Relationship between the (220), (200) and (1-11) plane. The [220] direction is perpendicular to the (220) plane and parallel with the line A1A2. The distance change between the (220) planes will lead to the length change along line A1A2 and A1B1. f) Atomic arrangement of NiO (111), Ni(OH)2 (001)and NiOOH (001) plane. The Ni-Ni distances for both Ni(OH)2 and NiOOH are higher than that of the NiO.

clear that the intensity of the Ni-O bond peak for the pristine sample after 1.6V is lower than that of the sodiated sample from the R space of Ni K edge EXAFS (Fig. 3e), which implies that the higher degree of amorphization for the pristine sample after 1.6V CA test. Although $Ni(OH)_2$ is formed for both pristine and sodiated samples after the CV test, there is a slight shift for the Ni K-edge in the k space for the sodiated sample tested at 1.6V vs. RHE (Fig. 3f). The difference may be originated from the different degrees of crystallinity at the surfaces.

We then perform synchrotron XRD on the pristine and sodiated samples after different CV cycles to investigate the influences of the different surface transformation. The XRD peaks are well aligned after the peak position calibration using the carbon paper substrate as the reference. No difference can be discerned for the XRD results of the pristine NiO sample with different cycles (Fig. 4a and S5). While for the sodiated sample, there are changes at both (200) and (220) peaks (Fig. 4b, 4c and 4d). The peaks associated with the Ni particles disappear after the CV test, indicating the complete phase change of the Ni particles during the CV cycles. No peaks representing Ni hydroxide/oxyhydroxide can be found after CV cycles, although the presence of Ni hydroxide/oxyhydroxide has been demonstrated by the redox couple before the OER take-off current (Fig. 2a, b) and the *operando* UV-vis test (Fig. 3a). The possible reason for the absence of the Ni hydroxide/oxyhydroxide XRD peaks is the XRD detection limitation for the relatively small amount of these phases. After 5 CV cycles, the peak representing (220) plane which is perpendicular to (1-11) plane (Fig. 4e) show a slightly shift to the left (Fig. 4c), indicating an expansion of the distance between the surface atoms at the (111) plane (Fig. 4e). As a result, the distance between the (200) planes also changed accordingly (Fig. 4d and 4e). After CV cycles, a Ni hydroxide/oxyhydroxide layer could be formed at the surface of the NiO. Due to the mismatch of the lattice parameters between Ni hydroxide/oxyhydroxide and NiO (Fig. 4f), a stress could be introduced at the interface, leading to the expansion of the distance between surface atoms in the NiO nanosheet. On the other hand, the lattice of the NiOOH produced during OER should experience a compressive stress, resulting in a contraction of the distance between the atoms in NiOOH at the interface. With more CV cycles, the (220) peak recovered to the original state. The possible reason is the release of the stress after too much surface transformation during CV cycling. The

behavior of the (220) peak shift is consistent with the OER performance variation, which implies that the OER performance enhancement during the initial 5 cycles is associated with the compressive stress caused by the coherent NiO/NiOOH structure, and the decrease of the performance afterward is origin from the release of the stress due to the excessive surface transformation. Our results not only demonstrated the possibilities of enhancing the OER performance through stress engineering and also uncover the challenges of maintain the stress due to the dynamic surface change of the material under OER conditions.

Conclusions

In conclusion, we report a crystalline surface transformation of a rocksalt NiO to layered NiOOH and investigate its influence on the OER performance. We first produce Ni/NiO interfaces through the battery conversion chemistry. The Ni particles can then be transformed to crystalline NiOOH through an *in situ* electrochemical transformation. Due to the lattice mismatch between NiO and the crystalline NiOOH, a compressive stress is introduced to the OER-active NiOOH. As a result, the adsorption energy for the intermediates are also adjusted accordingly, leading to ~20-fold enhancement of the OER performance. In the long-term CV cycling, however, the release of the compressive stress leads to the degradation of the OER performance. Our finding suggests that the OER performance of the Ni based hydroxide can be enhanced through a stable mechanical stress engineering

Conflicts of interest

There are no conflicts to declare.

Notes and references

Acknowledgements

The work was supported by Department of Chemistry startup funds and the Institute for Critical Technology and Applied Science. This work at Tianjin university was supported by the Natural Science Foundation of China (Nos. 51871160, 51671141, and 51471115). This research used the TEM resources of the UC Irvine Materials Research Institute (IMRI) and the Center for Functional Nanomaterials, which is a U.S. DOE Office of Science Facility, at Brookhaven National Laboratory under Contract No. DE-SC0012704. This research used resources of the Advanced Photon Source, a U.S. Department of Energy (DOE) Office of Science User Facility operated for the DOE Office of Science by Argonne National Laboratory under Contract No. DE-AC02-06CH11357. Use of the Stanford Synchrotron Radiation Lightsource, SLAC National Accelerator Laboratory, is supported by the US Department of Energy, Office of Science, Office of Basic Energy Sciences under Contract No.DE-AC02-76SF00515. F.L. thanks R. Richards and C. Cadigan for providing the NiO precursor.

Author contribution

F.L. conceived and supervised the project. C.K. and F.L. designed the experiments. C.K. performed electrochemistry, synchrotron XRD, hard XAS, TEM, and UV-Vis. F.L. performed the SEM experiment. Y.Z. and D.N. performed the soft XAS experiments. L.H. and H.L.L. performed the STEM experiments. C.-J.S. performed hard XAS experiments. C.K. was co-supervised by S.Q., X.-W.D. and F.L. C.K. and F.L. wrote the manuscript with the help from all coauthors.

Reference

1. K. L. Nardi, N. Yang, C. F. Dickens, A. L. Strickler and S. F. Bent, *Advanced Energy Materials*, 2015, **5**, 1500412.
2. D. U. Lee, J. Fu, M. G. Park, H. Liu, A. Ghorbani Kashkooli and Z. Chen, *Nano letters*, 2016, **16**, 1794-1802.
3. J. Yin, Y. Li, F. Lv, Q. Fan, Y. Q. Zhao, Q. Zhang, W. Wang, F. Cheng, P. Xi and S. Guo, *ACS nano*, 2017, **11**, 2275-2283.
4. L. Peng, J. Shen, X. Zheng, R. Xiang, M. Deng, Z. Mao, Z. Feng, L. Zhang, L. Li and Z. Wei, *Journal of Catalysis*, 2019, **369**, 345-351.
5. R. H. Zhang, T. S. Zhao, H. R. Jiang, M. C. Wu and L. Zeng, *Journal of Power Sources*, 2019, **409**, 76-85.
6. S. Zhan, Z. Zhou, M. Liu, Y. Jiao and H. Wang, *Catalysis Today*, 2019, **327**, 398-404.
7. J. Qian, X. Guo, T. Wang, P. Liu, H. Zhang and D. Gao, *Applied Catalysis B: Environmental*, 2019, **250**, 71-77.
8. H. Yang, Z. Chen, W. Hao, H. Xu, Y. Guo and R. Wu, *Applied Catalysis B: Environmental*, 2019, **252**, 214-221.
9. D. Jia, H. Gao, L. Xing, X. Chen, W. Dong, X. Huang and G. Wang, *Inorganic chemistry*, 2019, **58**, 6758-6764.
10. Z. W. Gao, J. Y. Liu, X. M. Chen, X. L. Zheng, J. Mao, H. Liu, T. Ma, L. Li, W. C. Wang and X. W. Du, *Advanced materials*, 2019, **31**, e1804769.
11. Z. W. Seh, J. Kibsgaard, C. F. Dickens, I. Chorkendorff, J. K. Norskov and T. F. Jaramillo, *Science*, 2017, **355**.
12. R. Paul, Q. Dai, C. Hu and L. Dai, *Carbon Energy*, 2019, **1**, 19-31.
13. H. Wang and Y. Cui, *Carbon Energy*, 2019, **1**, 13-18.
14. I. C. Man, H. Y. Su, F. Calle-Vallejo, H. A. Hansen, J. I. Martínez, N. G. Inoglu, J. Kitchin, T. F. Jaramillo, J. K. Nørskov and J. Rossmeisl, *ChemCatChem*, 2011, **3**, 1159-1165.
15. S. Deng, M. Luo, C. Ai, Y. Zhang, B. Liu, L. Huang, Z. Jiang, Q. Zhang, L. Gu, S. Lin, X. Wang, L. Yu, J. Wen, J. Wang, G. Pan, X. Xia and J. Tu, *Angewandte Chemie*, 2019, **58**, 16289-16296.
16. O. Diaz-Morales, I. Ledezma-Yanez, M. T. M. Koper and F. Calle-Vallejo, *ACS Catalysis*, 2015, **5**, 5380-5387.
17. Y.-F. Li and A. Selloni, *ACS Catalysis*, 2014, **4**, 1148-1153.
18. J. Y. Lin, C. Xi, Z. Li, Y. Feng, D. Y. Wu, C. K. Dong, P. Yao, H. Liu and X. W. Du, *Chemical communications*, 2019, **55**, 3121-3123.
19. L. Bu, N. Zhang, S. Guo, X. Zhang, J. Li, J. Yao, T. Wu, G. Lu, J.-Y. Ma, D. Su and X. Huang, *Science*, 2016, **354**, 1410-1414.

20. M. Escudero-Escribano, P. Malacrida, M. H. Hansen, U. G. Vej-Hansen, A. Velázquez-Palenzuela, V. Tripkovic, J. Schiøtz, J. Rossmeisl, I. E. L. Stephens and I. Chorkendorff, *Science*, 2016, **352**, 73-76.
21. H. Wang, S. Xu, C. Tsai, Y. Li, C. Liu, J. Zhao, Y. Liu, H. Yuan, F. Abild-Pedersen, F. B. Prinz, J. K. Nørskov and Y. Cui, *Science*, 2016, **354**, 1031-1036.
22. Y. Tong, Y. Guo, P. Chen, H. Liu, M. Zhang, L. Zhang, W. Yan, W. Chu, C. Wu and Y. Xie, *Chem*, 2017, **3**, 812-821.
23. J. Huang, J. Chen, T. Yao, J. He, S. Jiang, Z. Sun, Q. Liu, W. Cheng, F. Hu, Y. Jiang, Z. Pan and S. Wei, *Angewandte Chemie International Edition*, 2015, **54**, 8722-8727.
24. A. L. Xia, H. L. Zhang, L. N. Tong and B. S. Han, *Thin Solid Films*, 2008, **516**, 7653-7656.
25. A. M. Smith, A. M. Mohs and S. Nie, *Nature Nanotechnology*, 2009, **4**, 56-63.
26. L. Trotochaud, J. K. Ranney, K. N. Williams and S. W. Boettcher, *Journal of the American Chemical Society*, 2012, **134**, 17253-17261.
27. T. Wu, S. Sun, J. Song, S. Xi, Y. Du, B. Chen, W. A. Sasangka, H. Liao, C. L. Gan, G. G. Scherer, L. Zeng, H. Wang, H. Li, A. Grimaud and Z. J. Xu, *Nature Catalysis*, 2019, **2**, 763-772.
28. E. Fabbri, M. Nachtegaal, T. Binninger, X. Cheng, B. J. Kim, J. Durst, F. Bozza, T. Graule, R. Schaublin, L. Wiles, M. Pertoso, N. Danilovic, K. E. Ayers and T. J. Schmidt, *Nature materials*, 2017, **16**, 925-931.
29. A. Bergmann, T. E. Jones, E. Martinez Moreno, D. Teschner, P. Chernev, M. Gliech, T. Reier, H. Dau and P. Strasser, *Nature Catalysis*, 2018, **1**, 711-719.
30. B. R. Wygant, K. Kawashima and C. B. Mullins, *ACS Energy Letters*, 2018, **3**, 2956-2966.
31. S. Deng, Y. Shen, D. Xie, Y. Lu, X. Yu, L. Yang, X. Wang, X. Xia and J. Tu, *Journal of Energy Chemistry*, 2019, **39**, 61-67.
32. A. Grimaud, K. J. May, C. E. Carlton, Y. L. Lee, M. Risch, W. T. Hong, J. Zhou and Y. Shao-Horn, *Nature communications*, 2013, **4**, 2439.
33. F. Lin, D. Nordlund, T. C. Weng, Y. Zhu, C. Ban, R. M. Richards and H. L. Xin, *Nature communications*, 2014, **5**, 3358.
34. K. He, F. Lin, Y. Zhu, X. Yu, J. Li, R. Lin, D. Nordlund, T. C. Weng, R. M. Richards, X. Q. Yang, M. M. Doeff, E. A. Stach, Y. Mo, H. L. Xin and D. Su, *Nano letters*, 2015, **15**, 5755-5763.
35. M. Zhang, M. de Respinis and H. Frei, *Nature chemistry*, 2014, **6**, 362-367.
36. K. He, H. L. Xin, K. Zhao, X. Yu, D. Nordlund, T. C. Weng, J. Li, Y. Jiang, C. A. Cadigan, R. M. Richards, M. M. Doeff, X. Q. Yang, E. A. Stach, J. Li, F. Lin and D. Su, *Nano letters*, 2015, **15**, 1437-1444.
37. G. C. Giovanni CARTURAN, Stefano ENZO, Renzo GANZERLA and Maurizio LENARDA, *Materials Letters*, 1988, **7**, 47-50.
38. Q. L. Min Han, Jinghui He, You Song, Zheng Xu, and Jianming Zhu, *Adv. Mater.*, 2007, **19**.
39. B. J. Trzesniewski, O. Diaz-Morales, D. A. Vermaas, A. Longo, W. Bras, M. T. Koper and W. A. Smith, *Journal of the American Chemical Society*, 2015, **137**, 15112-15121.
40. M. Gorlin, P. Chernev, J. Ferreira de Araujo, T. Reier, S. Dresp, B. Paul, R. Krahnert, H. Dau and P. Strasser, *Journal of the American Chemical Society*, 2016, **138**, 5603-5614.
41. N. Li, D. K. Bediako, R. G. Hadt, D. Hayes, T. J. Kempa, F. V. Cube, D. C. Bell, L. X. Chen and D. G. Nocera, *PNAS*, 2017, **114**, 1486-1491.
42. C. Kuai, Y. Zhang, D. Wu, D. Sokaras, L. Mu, S. Spence, D. Nordlund, F. Lin and X.-W. Du, *ACS Catalysis*, 2019, **9**, 6027-6032.
43. M. Gorlin, P. Chernev, P. Paciok, C. W. Tai, J. Ferreira de Araujo, T. Reier, M. Heggen, R. Dunin-Borkowski, P. Strasser and H. Dau, *Chemical communications*, 2019, **55**, 818-821.
44. Z. X. Chunguang Kuai, Cong Xi, Zhijie Yang, Yan Zhang, Cheng-Jun Sun, Luxi Li, Dimosthenis Sokaras, Cunku Dong, Shizhang Qiao, Xi-Wen Du, Feng Lin, *Submitted,* 2020.

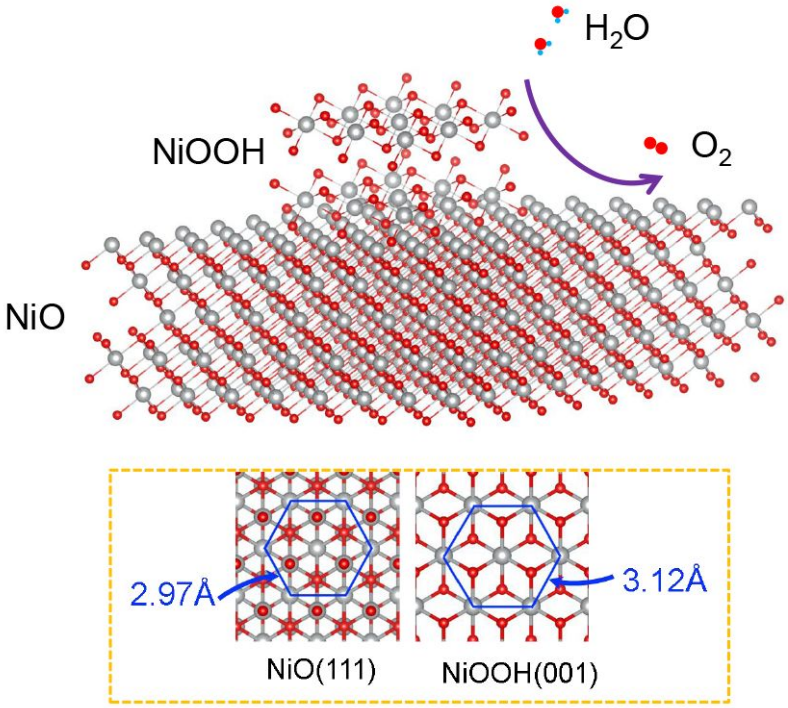

The compressive stress at the NiOOH/NiO interface, created through the battery conversion chemistry, is found to influence the OER performance.